

# Hybrid Photonic–Plasmonic Crystal Nanocavities

Xiaodong Yang,<sup>†,\*,§</sup> Atsushi Ishikawa,<sup>\*,§</sup> Xiaobo Yin,<sup>†,‡</sup> and Xiang Zhang<sup>†,\*,\*</sup>

<sup>†</sup>Materials Sciences Division, Lawrence Berkeley National Laboratory, 1 Cyclotron Road, Berkeley, California 94720, United States, and <sup>‡</sup>NSF Nanoscale Science and Engineering Center, 3112 Etcheverry Hall, University of California, Berkeley, California 94720, United States. <sup>§</sup> These authors contributed equally to this work.

Optical micro/nanocavities with both high  $Q$  and small  $V_m$  are of great importance in the enhancement of light–matter interaction.<sup>1,2</sup> The quality factor  $Q$  describes the spectral energy density of the cavity mode, which is proportional to the cavity photon lifetime. The mode volume  $V_m$  represents the spatial energy density of the cavity mode, which quantifies the electric field strength per photon. The long photon lifetime and strong light confinement in these high- $Q/V_m$  optical cavities lead to many fundamental studies of optical physics at nanoscale and integrated photonics applications, for example, enhanced spontaneous emission, strong coupling in cavity quantum electrodynamics (QED), enhancement of optical nonlinearities, and optomechanics.<sup>3–6</sup> Although conventional dielectric cavities can be designed to have ultrahigh  $Q$  factors, such as microspheres,<sup>7</sup> microtoroids,<sup>8</sup> and photonic crystal cavities,<sup>9</sup> the physical sizes of these cavities cannot be smaller than the wavelength scale in order to confine photon effectively. Therefore, the mode volumes for these dielectric cavities are diffraction-limited and are always larger than the single cubic wavelength  $(\lambda/n)^3$ .

Surface plasmon polaritons (SPPs) provide a new way to confine electromagnetic (EM) waves beyond the diffraction limit by storing the optical energy in free electron oscillations along the metal–dielectric interface.<sup>10,11</sup> The unique dispersion relation of SPPs supports high wave vectors with ultrashort wavelengths, resulting in different kinds of plasmonic nanocavities with subwavelength mode volumes and metal-loss-limited  $Q$  factors, such as plasmonic microdisk resonators,<sup>12</sup> metallic-fin Fabry–Pérot cavities,<sup>13</sup> and metallic-coated nanocavities for miniaturization of lasers.<sup>14–18</sup> With periodic dielectric lattice on the top of the metal layer, plasmonic crystals can be formed to support complete two-dimensional

**ABSTRACT** We propose a hybrid optical nanocavity consisting of photonic crystals coupled to a metal surface with a nanoscale air gap between. The hybridization of photonic crystal modes and surface plasmons across the gap forms hybrid cavity modes, which are highly confined in the low-loss air gap region. Deep subwavelength mode volume and high quality factor are demonstrated at telecommunication wavelength, resulting in an extremely large  $Q/V_m$  ratio of  $60\,000\,\lambda^{-3}$ . This new type of high- $Q/V_m$  broad-band hybrid nanocavity opens up opportunities for various applications in enhanced light–matter interactions.

**KEYWORDS:** optical nanocavity · photonic crystal · surface plasmon polariton · hybrid plasmonic mode

band gaps for SPP manipulation.<sup>19</sup> Plasmonic band gap nanocavities have also been proposed for confining light in deep subwavelength scale.<sup>20</sup> Although plasmonic cavities can achieve deep subwavelength mode volume, their quality factors are always limited by the parasitic loss of metal.

With the advantage of SPPs, a hybrid plasmonic waveguide has been proposed to squeeze optical energy into the nanoscale air gap between the dielectric waveguide and the metal surface.<sup>21</sup> In such a system, both deep subwavelength mode area and low propagation loss have been demonstrated for realizing nanophotonic applications such as nanolasers<sup>22</sup> and optical forces enhancement.<sup>23</sup> The confined optical energy can be boosted by introducing a high- $Q$  optical resonator to enhance the light–matter interactions further.<sup>24</sup> Hybrid plasmonic resonators based on total internal reflection (TIR) have been used to realize the low-threshold plasmonic nanolasers at room temperature.<sup>25</sup> In this paper, we propose a novel hybrid photonic–plasmonic crystal nanocavity by integrating photonic crystal structures into hybrid plasmonic waveguides, as illustrated in Figure 1. On the basis of the periodic variation in the effective index of hybrid mode, a unique hybrid photonic–plasmonic crystal with a transverse magnetic (TM) band gap is formed

\* Address correspondence to xiang@berkeley.edu.

Received for review December 7, 2010 and accepted March 8, 2011.

Published online March 08, 2011  
10.1021/nn1033482

© 2011 American Chemical Society

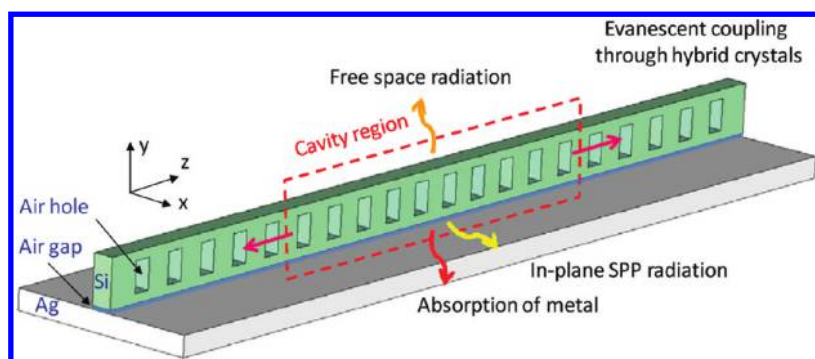


Figure 1. Schematic of the proposed hybrid photonic–plasmonic crystal nanocavity consisting of 10 lattice periods with parabolic variation of lattice constant in the cavity region. The photon loss channels of the hybrid crystal cavity modes include free space radiation, in-plane SPP radiation, evanescent coupling through hybrid crystals, and absorption of metal.

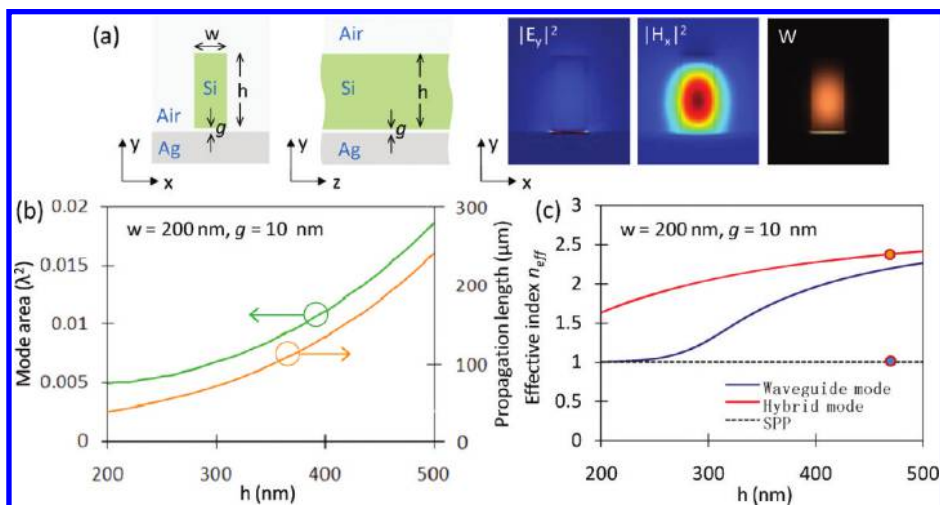


Figure 2. (a) Cross section of the hybrid plasmonic waveguide consisting of a rectangular silicon waveguide ( $w/h = 200/470$  nm) and silver substrate separated by an air gap ( $g = 10$  nm), and the distributions of electric field  $|E_y|^2$ , magnetic field  $|H_x|^2$ , and EM energy density  $W$  for the fundamental hybrid mode at 200 THz propagating along the  $z$ -axis. (b) Mode area  $A_m$  and the propagation length  $L_m$  of the hybrid mode as a function of the waveguide height  $h$ . (c) The  $h$  dependence of effective index  $n_{\text{eff}}$  for the hybrid mode (red curve), bare silicon waveguide mode (blue curve), and bare SPP mode (dotted curve).

at the telecommunication wavelength. One-dimensional hybrid crystal nanocavities having parabolic variation of lattice constant are then designed to realize both high- $Q$  factor and deep subwavelength mode volume  $V_m$ , which is due to the strong optical energy concentration in the low-loss air gap region. As shown in Figure 1, the photon loss channels of the hybrid crystal cavity mode include free space radiation, in-plane SPP radiation, evanescent coupling through hybrid crystals, and absorption of metal. We will systematically study the waveguide geometry dependences of radiation  $Q$  factor  $Q_{\text{rad}}$ , absorption  $Q$  factor  $Q_{\text{abs}}$ ,  $V_m$ , and  $Q/V_m$  in order to illustrate the mechanism of the optical confinement in such nanocavities. This new type of high- $Q/V_m$  broadband nanocavity will be of great importance in the enhancement of light–matter interactions, such as cavity QED, nonlinear optics, low-threshold nanoscale lasers, optomechanics, biological sensors,<sup>26,27</sup> and surface-enhanced Raman scattering (SERS).<sup>28–30</sup>

## RESULTS AND DISCUSSION

Figure 2a shows the geometry of the hybrid plasmonic waveguide consisting of a rectangular silicon waveguide coupled to a flat silver substrate with a nanoscale air gap  $g$  between. In Figure 2a, we also show the distributions of electric field  $|E_y|^2$ , magnetic field  $|H_x|^2$ , and EM energy density  $W$  for the fundamental hybrid mode at 200 THz propagating along the  $z$ -axis. The strong coupling between the silicon waveguide mode and the SPP mode results in the concentration of optical energy inside the low-loss air gap. Figure 2b shows the waveguide height  $h$  dependence of the mode area  $A_m$  and the propagation length  $L_m$  of the hybrid mode with waveguide width  $w = 200$  nm and gap  $g = 10$  nm. The strong optical confinement of the hybrid mode into the nanoscale air gap results in an ultrasmall mode area down to  $0.005 \lambda^2$ . At the same time, the hybrid mode can travel through a long distance, which is more than  $40 \mu\text{m}$  at 200 THz.

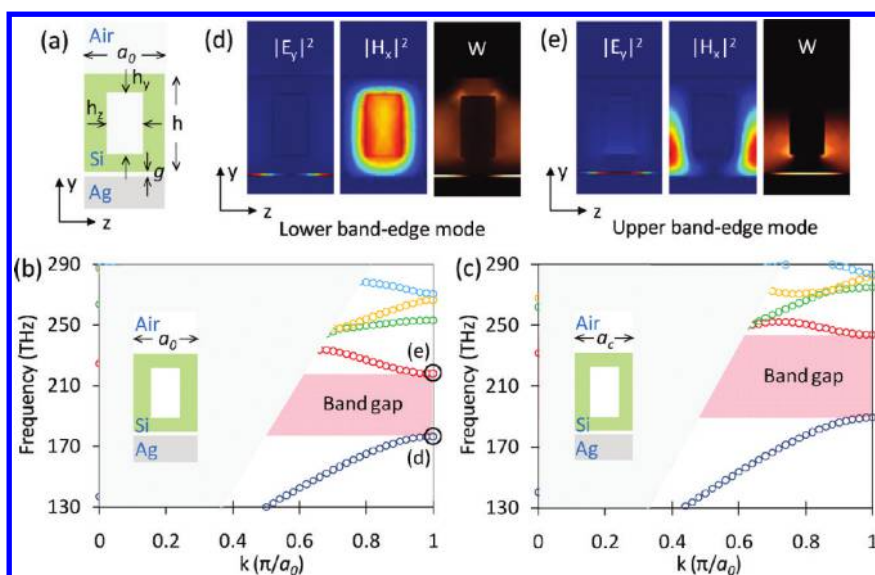


Figure 3. (a) Unit cell of one-dimensional hybrid photonic–plasmonic crystal with a rectangular air hole located inside the silicon waveguide. The TM band structure of the hybrid crystal for the lattice constant (b)  $a_0 = 420$  nm and (c)  $a_c = 0.9a_0$ . The light cone is indicated by the gray region. The corresponding field distributions ( $|E_y|^2$ ,  $|H_x|^2$ , and  $W$ ) of lower band-edge mode (d) and upper band-edge mode (e) at the Brillouin zone boundary in (b).

Figure 2c plots the  $h$  dependence of effective index  $n_{\text{eff}}$  for the hybrid mode (red curve), bare silicon waveguide mode (blue curve), and bare SPP mode (dotted curve). Note that the effective index of an optical mode characterizes the phase velocity of the eigenmode propagating along the  $z$  direction.<sup>21</sup> For example, when  $h = 470$  nm, the effective index of the hybrid mode is  $n_{\text{eff}} = 2.3735$ , which is much larger than the refractive index of the SPP mode at the air–silver interface, where  $n_{\text{SPP}} = (\epsilon_m \epsilon_d / (\epsilon_m + \epsilon_d))^{1/2} = 1.0039$ . This high index contrast ensures the formation of a hybrid photonic–plasmonic crystal with a TM band gap by introducing photonic crystal structure into the silicon waveguide.

Figure 3a shows the unit cell of a hybrid photonic–plasmonic crystal by introducing periodic rectangular air holes inside the silicon waveguide along the  $z$ -axis. The lattice constant is  $a_0 = 420$  nm, and the dimensions of the air hole are  $h_y = 0.626h$  and  $h_z = 0.4a_0$ . In Figure 3b, we show the band structure of the hybrid crystal for TM polarization. A band gap is clearly visible from 176 to 218 THz indicated by the red area, while some higher order modes form the band structure below the light cone (marked by the gray region). Panels d and e of Figure 3 plot the corresponding field distributions ( $|E_y|^2$ ,  $|H_x|^2$ , and  $W$ ) of lower band-edge mode (at 176 THz) and upper band-edge mode (at 218 THz) at the Brillouin zone boundary, respectively. The electric field is mostly located in the high effective index region for the lower band-edge mode, whereas the electric field for the upper band-edge mode is concentrated underneath the air hole with low effective index. Figure 3c shows the band structure of the same hybrid crystal but with a smaller lattice constant

$a_c = 0.9a_0$ . The band gap will shift to higher frequencies, which is from 189 to 244 THz, due to the reduced effective index as the optical modes have more overlap with air. As a result, by combining these two hybrid crystal structures, the lower band-edge mode with lattice constant  $a_c$  lies within the band gap of the unit cell with lattice constant  $a_0$ , which will act as the defect cavity mode trapped inside the  $a_0$  lattice. This mechanism of light confinement in mode-gap cavities has been demonstrated to realize ultrahigh  $Q$  factor in dielectric photonic crystal cavities.<sup>31–33</sup>

On the basis of the band structure of the hybrid crystal, we have designed a hybrid crystal nanocavity to support the cavity modes highly confined two-dimensionally along both the  $x$  and  $y$  directions, as shown in Figure 1 and Figure 4a. In order to construct an optical potential well to trap the optical modes along the  $z$ -axis, we introduced a parabolic relationship in the lattice constant with the lattice number  $N$  from  $a_0$  to  $a_c = 0.9a_0$ .<sup>32,33</sup> This gradual lattice variation dramatically reduces the mode profile mismatch between the Bloch modes in the cavity and the mirror, so as to address high radiation  $Q$  factors. The perturbations of lattice constants span five periods away from the cavity center, so that the cavity region covers 10 lattice periods, as illustrated in Figure 4b. The corresponding lower and upper band-edge frequencies for different lattice number along the  $z$ -axis are plotted in Figure 4c. The acceptor-type defect cavity is clearly formed at the Brillouin zone boundary, which supports two eigenmodes in the mode gap. Figure 4d,e illustrates the field distributions of  $E_y$ ,  $|E|^2$ , and  $W$  for two eigenmodes supported in this cavity, with resonant frequencies of 184 THz for the first order mode ( $m = 1$ )

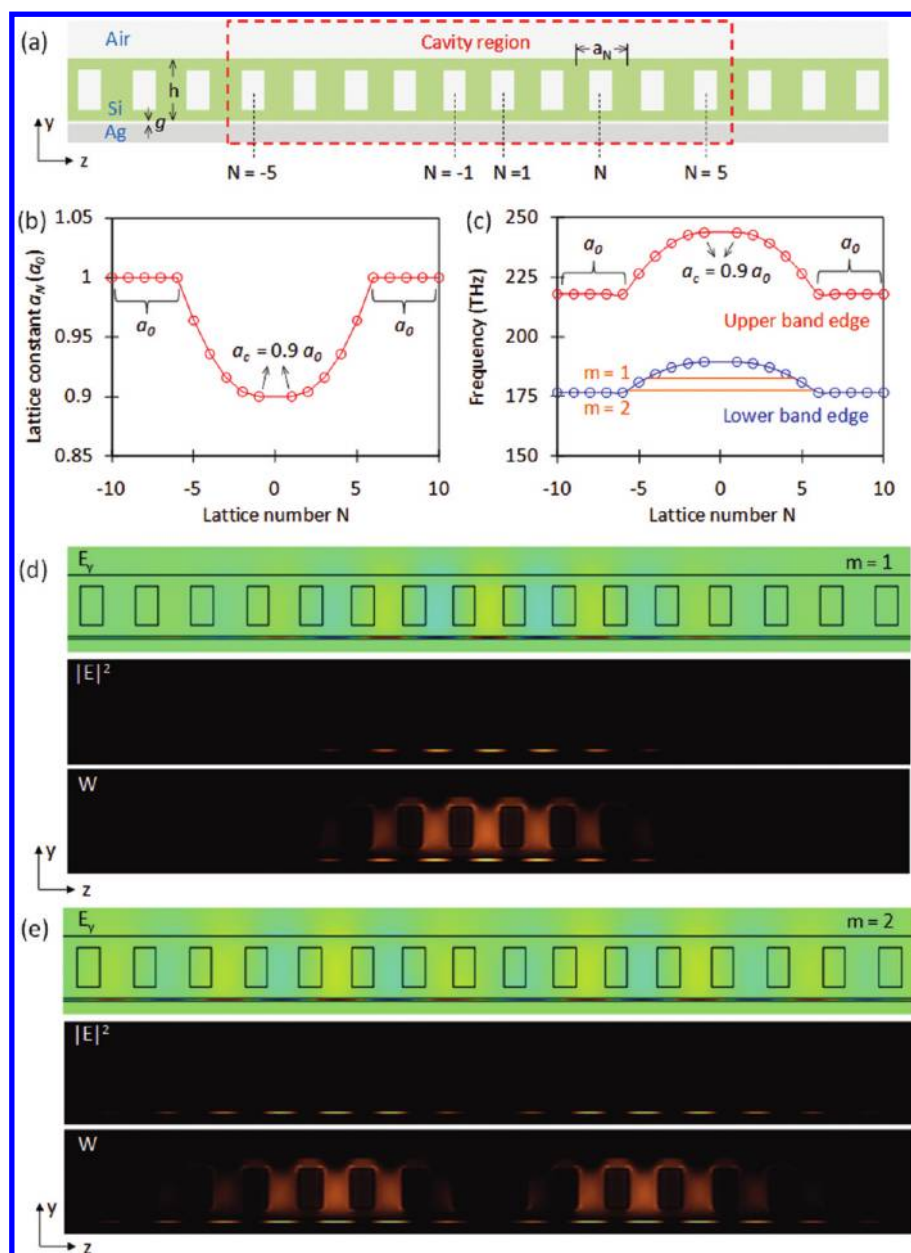


Figure 4. (a) Schematic of the hybrid crystal nanocavity consisting of 10 lattice periods in the cavity region. (b) Lattice constant  $a_N$  along the waveguide as a parabolic function of the lattice number  $N$  from  $a_0$  to  $a_c = 0.9a_0$ . (c) Lower and upper band-edge frequencies along the waveguide. The created acceptor-type cavity supports two eigenmodes ( $m = 1$  and  $m = 2$ ) inside the mode gap. The corresponding field distributions ( $E_y$ ,  $|E|^2$ , and  $W$ ) for the two eigenmodes (d)  $m = 1$  and (e)  $m = 2$  of hybrid crystal cavity with  $g = 10$  nm.

with even symmetry respect to the  $x$ - $y$  plane and 178 THz for the second order mode ( $m = 2$ ) with odd symmetry. The electrical field intensity  $|E|^2$  is strongly squeezed inside the low-loss air gap, while most of the EM energy density  $W$  is also concentrated inside the gap region. The modes are confined within only several lattice periods in the cavity region along the  $z$ -axis. The total quality factors  $Q_{\text{tot}}$  reach 457 and 338 for the first-order mode and the second-order mode, respectively.  $1/Q_{\text{tot}} = 1/Q_{\text{rad}} + 1/Q_{\text{abs}}$ , where  $Q_{\text{rad}}$  is the radiation  $Q$  factor and  $Q_{\text{abs}}$  is the absorption  $Q$  factor due to the ohmic loss of the metal. The mode volume  $V_m$  is around

2 orders of magnitude smaller than the wavelength cubic, which is  $0.0092 (\lambda/n_{\text{air}})^3$  and  $0.0122 (\lambda/n_{\text{air}})^3$  for each mode.

Figure 5 shows the dependences of quality factor  $Q$ , mode volume  $V_m$ , and the  $Q_{\text{tot}}/V_m$  ratio on the gap separation  $g$  for the waveguide with  $w = 200$  nm and  $h = 470$  nm. For  $m = 1$  mode plotted in Figure 5a, as  $g$  is increased from 0 to 50 nm,  $Q_{\text{abs}}$  increases almost linearly because the coupling between the silicon waveguide mode and SPPs is getting weaker so that the energy loss inside the metal is reduced. When  $g = 0$ , the pure plasmonic crystal cavity mode shown in



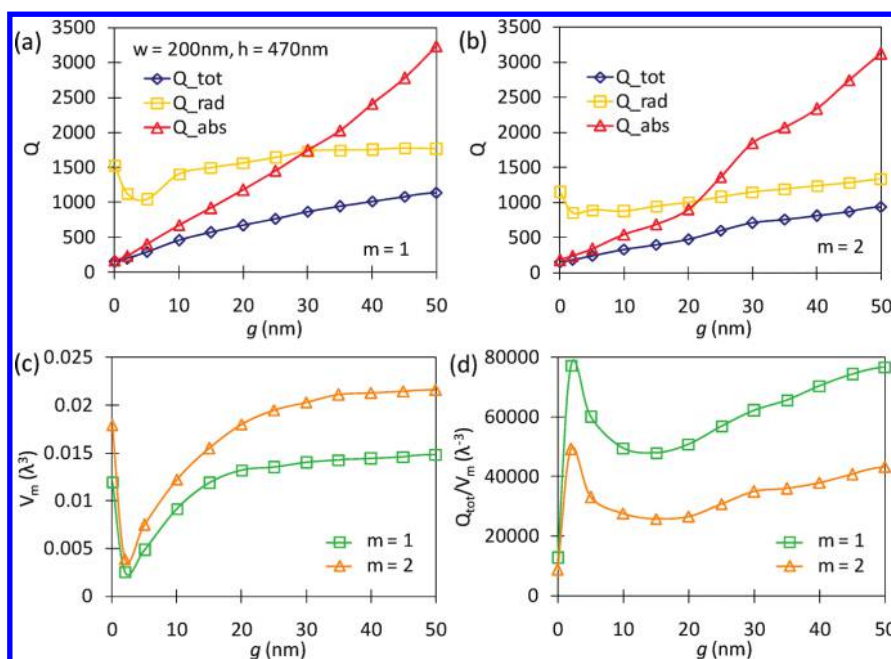


Figure 5. Dependences of quality factors  $Q_{\text{tot}}$ ,  $Q_{\text{rad}}$ , and  $Q_{\text{abs}}$  on the gap separation  $g$  with  $w = 200$  nm and  $h = 470$  nm for the two eigenmodes (a)  $m = 1$  and (b)  $m = 2$ . (c) Mode volume  $V_m$  and (d)  $Q_{\text{tot}}/V_m$  ratio as a function of air gap  $g$  for the two eigenmodes.

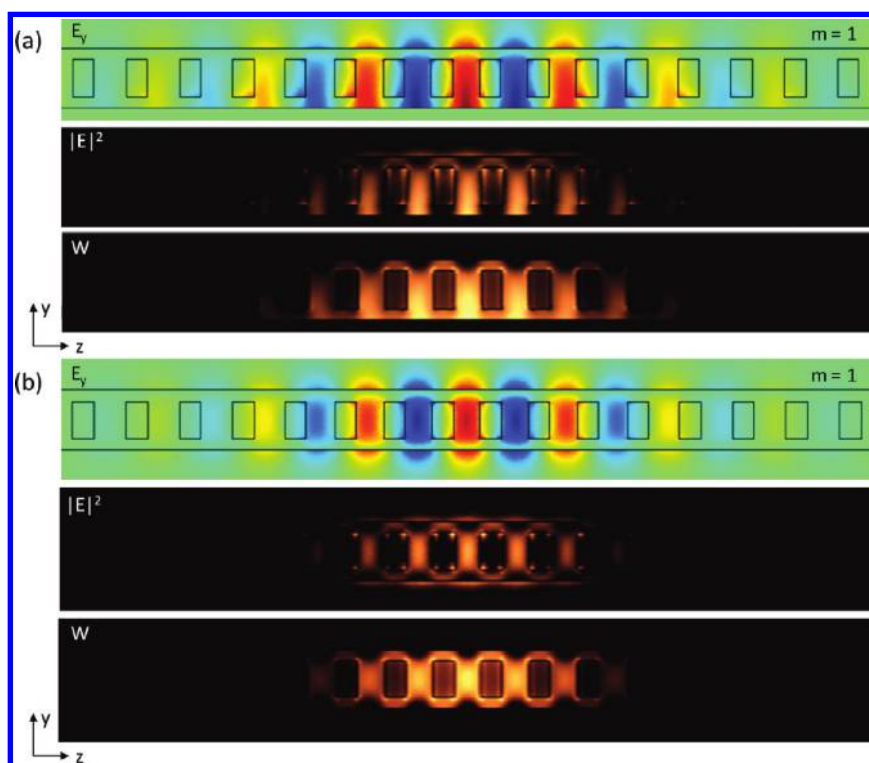


Figure 6. (a) Field distributions ( $E_y$ ,  $|E|^2$ , and  $W$ ) for  $m = 1$  mode of pure plasmonic crystal cavity ( $g = 0$ ). (b) Field distributions ( $E_y$ ,  $|E|^2$ , and  $W$ ) for  $m = 1$  mode of conventional dielectric photonic crystal cavity ( $g = \infty$ ).

Figure 6a suffers from the largest absorption loss of the metal. On the other hand,  $Q_{\text{rad}}$  slightly increases for the hybrid cavity mode as  $g$  changes from 2 to 50 nm because the free space radiation due to the optical scattering from the air gap and the radiation coupled

to the in-plane SPP radiation are slightly reduced as the air gap gets larger. The radiation loss is mostly determined by the hybrid crystal structure and weakly depends on the coupling between the dielectric waveguide mode and the SPP mode, which is limited by

the  $Q_{\text{rad}}$  of dielectric photonic crystal cavity mode shown in Figure 6b (where  $Q_{\text{rad}} \sim 1525$ ). The pure plasmonic crystal cavity mode has a relatively higher  $Q_{\text{rad}}$  compared to the hybrid crystal cavity mode, due to the absence of the optical scattering from the air gap.  $Q_{\text{abs}}$  dominates the optical loss when  $g < 30$  nm.  $Q_{\text{tot}}$  gradually increase from 153 to 1140 as the gap varies from 0 to 50 nm. As plotted in Figure 5c, the mode volume  $V_m$  for  $m = 1$  mode of hybrid crystal cavity can be above 2 orders of magnitude smaller than the wavelength cubic. For example, at  $g = 2$  nm, hybrid crystal cavity mode has  $V_m$  of  $0.0025 (\lambda/n_{\text{air}})^3$ . As a comparison, pure plasmonic crystal cavity mode has a large  $V_m$  of  $0.51 (\lambda/n_{\text{si}})^3$ , and dielectric photonic crystal cavity mode also has a similar  $V_m$  of  $0.64 (\lambda/n_{\text{si}})^3$  because the optical energy is mostly confined in the high-index dielectric structures for both cases, which are above 200 times larger than the mode volume of hybrid crystal cavity mode. As a result, the nanoscale air gap is essential in the proposed system to support the hybrid mode for the deep subwavelength  $V_m$  and improved  $Q_{\text{tot}}$ . The figure of merit for optical cavities

**TABLE 1. Lattice Constant  $a_0$ , Hole Size  $h_y$  and  $h_z$  for Different Waveguide Height  $h$  in Figure 7**

$h$ (nm)	$a_0$ (nm)	$h_y (\times h)$	$h_z (\times a_0)$
250	730	0.5	0.7
300	650	0.6	0.65
350	570	0.6	0.6
400	490	0.6	0.5
470	420	0.626	0.4

$Q_{\text{tot}}/V_m$  ratio is then plotted in Figure 5d. The plasmonic crystal cavity mode has a  $Q_{\text{tot}}/V_m$  ratio of 300  $(\lambda/n_{\text{si}})^{-3}$ , and the dielectric photonic crystal cavity mode has 2400  $(\lambda/n_{\text{si}})^{-3}$  for  $m = 1$  mode, while the  $Q_{\text{tot}}/V_m$  ratio of hybrid crystal cavity mode is above 48 000  $(\lambda/n_{\text{air}})^{-3}$  with a maximum value of 77 000  $(\lambda/n_{\text{air}})^{-3}$  at  $g = 2$  nm. This ultralarge  $Q_{\text{tot}}/V_m$  ratio will significantly increase the Purcell factor and enhance the spontaneous emission rate for emitters in the cavity center.<sup>34</sup> The  $m = 2$  mode has a lower  $Q_{\text{rad}}$  because its resonant frequency is close to the lower band edge of the band gap, as shown in Figure 4c, leading to large evanescent coupling through hybrid crystals along the  $z$  direction. The mode volume of the  $m = 2$  mode is slightly larger than the  $m = 1$  mode, due to the broadening of the mode distribution along the  $z$ -axis.

Even larger  $Q_{\text{tot}}/V_m$  ratio can be obtained by tuning the waveguide height  $h$ . According to Figure 2c, as  $h$  is increased, the effective index  $n_{\text{eff}}$  for the hybrid mode gets larger (shown in the red curve), leading to lower resonant frequencies of the cavity modes. To systematically study the  $h$  dependences of  $Q$  and  $V_m$  at the same frequency region, we also tuned the lattice constant  $a_0$  and the hole size  $h_y$  and  $h_z$  for different waveguide height  $h$ , as listed in Table 1. Figure 7a plots the calculated band-edge frequencies and the resonant frequencies of two eigenmodes for various waveguide height  $h$  with  $w = 200$  nm and  $g = 10$  nm. Figure 7b–d shows the dependences of  $Q$ ,  $V_m$ , and  $Q_{\text{tot}}/V_m$  ratio on  $h$  for  $m = 1$  mode. As  $h$  varies from 250 to 470 nm, the effective index gets larger and more optical energy is located inside the dielectric waveguide

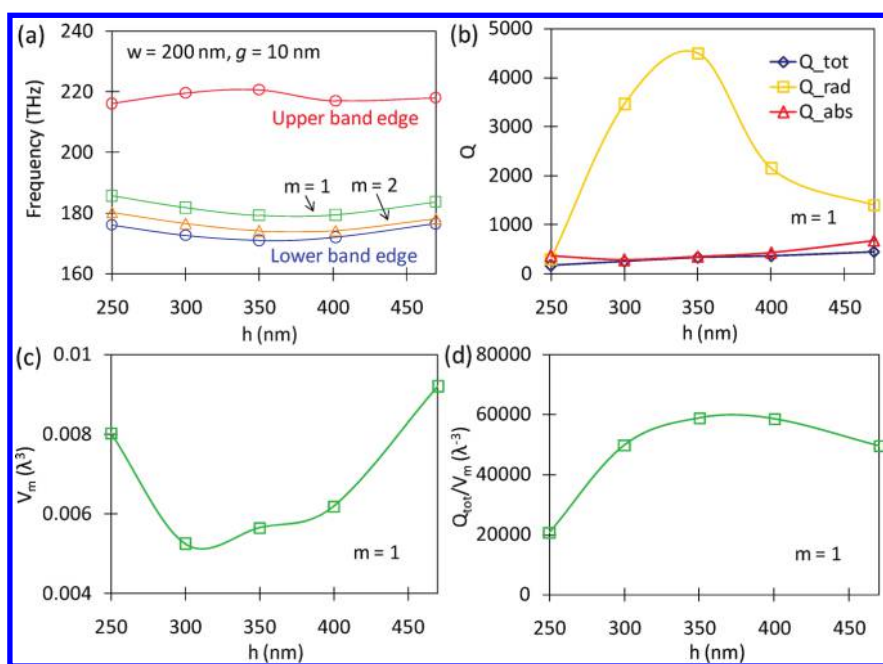


**Figure 7.** (a) Calculated band-edge frequencies and the resonant frequencies of two eigenmodes for various waveguide height  $h$  with  $w = 200$  nm and  $g = 10$  nm. The dependences of quality factors  $Q_{\text{tot}}$ ,  $Q_{\text{rad}}$ , and  $Q_{\text{abs}}$  (b), the mode volume  $V_m$  (c), and the  $Q_{\text{tot}}/V_m$  ratio (d) on  $h$  for  $m = 1$  mode.

mode, which results in the reduced metal loss and the slight increase of  $Q_{\text{abs}}$ , as shown in Figure 7b.  $Q_{\text{rad}}$  reaches its maxima of 4500 at  $h = 350$  nm with  $a_0 = 570$  nm. Although absorption in the metal always dominates the optical energy loss,  $Q_{\text{tot}}$  can be as high as 330 at  $h = 350$  nm. The strong optical confinement gives a deep sub-wavelength mode volume of  $0.0056 (\lambda/n_{\text{air}})^3$  at  $h = 350$  nm, resulting in an extremely large  $Q_{\text{tot}}/V_{\text{m}}$  of 60 000  $(\lambda/n_{\text{air}})^{-3}$ , as shown in Figure 7c,d. The enhancement of the spontaneous emission rate of a radiating dipole into the cavity mode with a perfect spatial and spectral matching, compared to the emission rate in the bulk material, can be described by the Purcell factor<sup>34,35</sup>

$$F_{\text{p}} = \frac{3}{4\pi^2} \left( \frac{\lambda}{n} \right)^3 \left( \frac{Q_{\text{tot}}}{V_{\text{m}}} \right)$$

where  $n$  is the index of refraction at the field intensity maximum. Our proposed system can achieve  $F_{\text{p}} \approx 4560$  for the cavity having  $Q_{\text{tot}}/V_{\text{m}}$  of 60 000  $(\lambda/n_{\text{air}})^{-3}$  and  $n = n_{\text{air}}$ , with the waveguide geometry of  $w = 200$  nm,  $h = 350$  nm, and  $g = 10$  nm. The  $Q_{\text{tot}}$  can be increased further by reducing the temperature, where the damping

collision frequency of the free electrons in the metal is decreased so that a larger Purcell factor may be achieved.<sup>14–16</sup> SERS signal from a single molecule can also be significantly improved with the current hybrid crystal nanocavity since the enhancement of both the incoming pump light and the scattered Stokes signal are proportional to  $Q_{\text{tot}}^2/V_{\text{m}}$  and a giant increase of the Raman scattering cross section for the molecule can be achieved.<sup>28</sup>

## CONCLUSION

We have proposed a hybrid photonic–plasmonic crystal nanocavity to achieve both deep subwavelength mode volume and high quality factor. High quality factor  $Q_{\text{tot}}$  of 330 and deep subwavelength mode volume  $V_{\text{m}}$  of  $0.0056 \lambda^3$  are demonstrated at telecommunication wavelength. The calculated Purcell factor is as high as 4560 with an extremely large  $Q_{\text{tot}}/V_{\text{m}}$  of 60 000  $\lambda^{-3}$ . This new type of broad-band hybrid nanocavity can be used to realize many exciting applications in enhanced light–matter interactions, such as cavity QED, nanolasers, optomechanics, biological sensors, and SERS.

## METHODS

**Numerical Simulations.** The calculations are performed using the finite-element method (FEM) software package (COMSOL) with  $n_{\text{si}} = 3.5$  and the empirical value for  $n_{\text{Ag}}$  based on the Drude model,<sup>36</sup> where  $\epsilon_{\text{Ag}} = \epsilon_{\infty} - \omega_{\text{p}}^2/(\omega^2 - i\omega\gamma)$  with background dielectric constant  $\epsilon_{\infty} = 5.0$ , plasma frequency  $\omega_{\text{p}} = 1.38 \times 10^{16}$  rad/s, and collision frequency  $\gamma = 5.07 \times 10^{13}$  rad/s. The mode area for the hybrid plasmonic waveguide is calculated from  $A_{\text{m}} = W_{\text{m}}/\max[W(\vec{r})]$ , where  $W_{\text{m}}$  is the integrated EM energy over the entire space  $W_{\text{m}} = \int \int W(\vec{r}) d^2r$ , and  $W(\vec{r})$  is the local EM energy density at the position  $\vec{r}$ , taking into account the strongly dispersive property of silver,<sup>12</sup> such that

$$W(\vec{r}) = \frac{1}{2} \left[ \text{Re} \left[ \frac{d(\omega\epsilon)}{d\omega} \right] |\vec{E}(\vec{r})|^2 + \mu |\vec{H}(\vec{r})|^2 \right]$$

The mode volume of the hybrid photonic–plasmonic nanocavity is calculated as

$$V_{\text{m}} = \frac{W_{\text{m}}}{\max[W(\vec{r})]} = \frac{1}{\max[W(\vec{r})]} \int \int \int W(\vec{r}) d^3r$$

The  $Q$  factors of the cavity modes are calculated from the formula  $Q = f_{\text{R}}/\Delta f$ , with the resonance frequency  $f_{\text{R}}$  and the full width at half-maximum (fwhm) of the resonance intensity spectrum  $\Delta f$ , which are calculated from the full wave simulations using the finite-difference time-domain method (CST Microwave Studio). The radiation  $Q$  factor can be calculated and separated from the absorption  $Q$  factor due to the metal loss by removing the imaginary part of the permittivity of silver.

**Acknowledgment.** This work was supported by the U.S. Department of Energy under Contract No. DE-AC02-05CH11231.

## REFERENCES AND NOTES

1. Yamamoto, Y.; Slusher, R. E. Optical Processes in Microcavities. *Phys. Today* **1993**, *46*, 66–73.

2. Vahala, K. J. Optical Microcavities. *Nature* **2003**, *424*, 839–846.
3. Noda, S.; Fujita, M.; Asano, T. Spontaneous-Emission Control by Photonic Crystals and Nanocavities. *Nat. Photonics* **2007**, *1*, 449–458.
4. Yoshie, T.; Scherer, A.; Hendrickson, J.; Khitrova, G.; Gibbs, H. M.; Rupper, G.; Ell, C.; Shchekin, O. B.; Deppe, D. G. Vacuum Rabi Splitting with a Single Quantum Dot in a Photonic Crystal Nanocavity. *Nature* **2004**, *432*, 200–203.
5. Soljacic, M.; Joannopoulos, J. D. Enhancement of Nonlinear Effects Using Photonic Crystals. *Nat. Mater.* **2004**, *3*, 211–219.
6. Kippenberg, T. J.; Vahala, K. J. Cavity Optomechanics: Back-Action at the Mesoscale. *Science* **2008**, *321*, 1172.
7. Spillane, S. M.; Kippenberg, T. J.; Vahala, K. J. Ultralow-Threshold Raman Laser Using a Spherical Dielectric Microcavity. *Nature* **2002**, *415*, 621–623.
8. Armani, D. K.; Kippenberg, T. J.; Spillane, S. M.; Vahala, K. J. Ultra-High-Q Toroid Microcavity on a Chip. *Nature* **2003**, *421*, 925–928.
9. Akahane, Y.; Asano, T.; Song, B. S.; Noda, S. High-Q Photonic Nanocavity in a Two-Dimensional Photonic Crystal. *Nature* **2003**, *425*, 944–947.
10. Barnes, W. L.; Dereux, A.; Ebbesen, T. W. Surface Plasmon Subwavelength Optics. *Nature* **2003**, *424*, 824–830.
11. Schuller, J. A.; Barnard, E. S.; Cai, W.; Jun, Y. C.; White, J. S.; Brongersma, M. L. Plasmonics for Extreme Light Concentration and Manipulation. *Nat. Mater.* **2010**, *9*, 193.
12. Min, B.; Ostby, E.; Sorger, V.; Ulin-Avila, E.; Yang, L.; Zhang, X.; Vahala, K. High-Q Surface-Plasmon-Polariton Whispering-Gallery Microcavity. *Nature* **2009**, *457*, 455–458.
13. Sorger, V. J.; Oulton, R. F.; Yao, J.; Bartal, G.; Zhang, X. Plasmonic Fabry-Pérot Nanocavity. *Nano Lett.* **2009**, *9*, 3489.
14. Hill, M. T.; Oei, Y.-S.; Smalbrugge, B.; Zhu, Y.; de Vries, T.; van Veldhoven, P. J.; van Otten, F. W. M.; Eijkemans, T. J.; Turkiewicz, J. P.; de Waardt, H.; Geluk, E. J.; Kwon, S.-H.; Lee, Y.-H.; Nötzel, R.; Smit, M. K. Lasing in Metallic-Coated Nanocavities. *Nat. Photonics* **2007**, *1*, 589–594.
15. Seo, M.; Kwon, S.; Ee, H.-S.; Park, H.-G. Full Three-Dimensional Subwavelength High-Q Surface-Plasmon-Polariton Cavity. *Nano Lett.* **2009**, *9*, 4078.

16. Kwon, S.; Kang, J.; Seassal, C.; Kim, S.; Regreny, P.; Lee, Y. H.; Lieber, C. M.; Park, H.-G. Subwavelength Plasmonic Lasing from a Semiconductor Nanodisk with Silver Nanoparticle Cavity. *Nano Lett.* **2010**, *10*, 3679–3683.
17. Nezhad, M. P.; Simic, A.; Bondarenko, O.; Slutsky, B.; Mizrahi, A.; Feng, L.; Lomakin, V.; Fainman, Y. Room-Temperature Subwavelength Metallo-Dielectric Lasers. *Nat. Photonics* **2010**, *4*, 395–399.
18. Yu, K.; Lakhani, A.; Wu, M. C. Subwavelength Metal-Optic Semiconductor Nanopatch Lasers. *Opt. Express* **2010**, *18*, 8790–8799.
19. Feng, L.; Lu, M. H.; Lomakin, V.; Fainman, Y. Plasmonic Photonic Crystal with a Complete Band Gap for Surface Plasmon Polariton Waves. *Appl. Phys. Lett.* **2008**, *93*, 231105.
20. Kim, M.; Lee, S. H.; Choi, M.; Ahn, B. H.; Park, N.; Lee, Y. H.; Min, B. Low-Loss Surface-Plasmonic Nanobeam Cavities. *Opt. Express* **2010**, *18*, 11089–11096.
21. Oulton, R. F.; Sorger, V.; Genov, D. A.; Pile, D. F. P.; Zhang, X. A Hybrid Plasmonic Waveguide for Subwavelength Confinement and Long-Range Propagation. *Nat. Photonics* **2008**, *2*, 496.
22. Oulton, R. F.; Sorger, V. J.; Zentgraf, T.; Ma, R.-M.; Gladden, C.; Dai, L.; Bartal, G.; Zhang, X. Plasmon Lasers at Deep Subwavelength Scale. *Nature* **2009**, *461*, 629–632.
23. Yang, X.; Liu, Y.; Oulton, R. F.; Yin, X.; Zhang, X. Optical Forces in Hybrid Plasmonic Waveguides. *Nano Lett.* **2011**, *11*, 321–328.
24. Xiao, Y.-F.; Li, B.-B.; Jiang, X.; Hu, X.; Li, Y.; Gong, Q. High Quality Factor, Small Mode Volume, Ring-Type Plasmonic Microresonator on a Silver Chip. *J. Phys. B: At., Mol. Opt. Phys.* **2010**, *43*, 035402.
25. Ma, R.-M.; Oulton, R. F.; Sorger, V. J.; Bartal, G.; Zhang, X. Room Temperature Sub-Diffraction-Limited Plasmon Laser by Total Internal Reflection. *Nat. Mater.* **2011**, *10*, 110.
26. Sun, C.; Su, K.-H.; Valentine, J.; Rosa-Bauza, Y. T.; Ellman, J. A.; Elboudwarej, O.; Mukherjee, B.; Craik, C. S.; Shuman, M. A.; Chen, F. F.; Zhang, X. Time-Resolved Single-Step Protease Activity Quantification Using Nanoplasmonic Resonator Sensors. *ACS Nano* **2010**, *4*, 978–984.
27. McPhillips, J.; Murphy, A.; Jonsson, M. P.; Hendren, W. R.; Atkinson, R.; Hook, F.; Zayats, A. V.; Pollard, R. J. High-Performance Biosensing Using Arrays of Plasmonic Nanotubes. *ACS Nano* **2010**, *4*, 2210–2216.
28. Maier, S. A. Plasmonic Field Enhancement and SERS in the Effective Mode Volume Picture. *Opt. Express* **2006**, *14*, 1957–1964.
29. Lee, S. Y.; Hung, L.; Lang, G. S.; Cornett, J. E.; Mayergoyz, I. D.; Rabin, O. Dispersion in the SERS Enhancement with Silver Nanocube Dimers. *ACS Nano* **2010**, *4*, 5763–5772.
30. Gehan, H.; Fillaud, L.; Chehimi, M. M.; Aubard, J.; Hohenau, A.; Felidj, N.; Mangeney, C. Thermo-Induced Electromagnetic Coupling in Gold/Polymer Hybrid Plasmonic Structures Probed by Surface-Enhanced Raman Scattering. *ACS Nano* **2010**, *4*, 6491–6500.
31. Song, B.-S.; Noda, S.; Asano, T.; Akahane, Y. Ultra-High-Q Photonic Double-Heterostructure Nanocavity. *Nat. Mater.* **2005**, *4*, 207.
32. Notomi, M.; Kuramochi, E.; Taniyama, H. Ultrahigh-Q Nanocavity with 1D Photonic Gap. *Opt. Express* **2008**, *16*, 11095.
33. Chan, J.; Eichenfield, M.; Camacho, R.; Painter, O. Optical and Mechanical Design of a 'Zipper' Photonic Crystal Optomechanical Cavity. *Opt. Express* **2009**, *17*, 3802.
34. Robinson, J. T.; Manolatu, C.; Chen, L.; Lipson, M. Ultra-small Mode Volumes in Dielectric Optical Microcavities. *Phys. Rev. Lett.* **2005**, *95*, 143901.
35. Purcell, E. M. Spontaneous Emission Probabilities at Radio Frequencies. *Phys. Rev.* **1946**, *69*, 681.
36. Johnson, P. B.; Christie, R. W. Optical Constants of the Noble Metals. *Phys. Rev. B* **1972**, *6*, 4370.